








Transition metal migration and O₂ formation underpin voltage hysteresis in oxygen-redox disordered rocksalt cathodes

Received: 3 February 2022

Accepted: 25 August 2022

Published online: 07 September 2022

 Check for updates

Kit McColl ^{1,2}, Robert A. House ^{2,3}, Gregory J. Rees ^{2,3}, Alexander G. Squires¹, Samuel W. Coles ^{1,2}, Peter G. Bruce ^{2,3,4}, Benjamin J. Morgan^{1,2} & M. Saiful Islam ^{1,2,3} 

Lithium-rich disordered rocksalt cathodes display high capacities arising from redox chemistry on both transition-metal ions (TM-redox) and oxygen ions (O-redox), making them promising candidates for next-generation lithium-ion batteries. However, the atomic-scale mechanisms governing O-redox behaviour in disordered structures are not fully understood. Here we show that, at high states of charge in the disordered rocksalt Li₂MnO₂F, transition metal migration is necessary for the formation of molecular O₂ trapped in the bulk. Density functional theory calculations reveal that O₂ is thermodynamically favoured over other oxidised O species, which is confirmed by resonant inelastic X-ray scattering data showing only O₂ forms. When O-redox involves irreversible Mn migration, this mechanism results in a path-dependent voltage hysteresis between charge and discharge, commensurate with the hysteresis observed electrochemically. The implications are that irreversible transition metal migration should be suppressed to reduce the voltage hysteresis that afflicts O-redox disordered rocksalt cathodes.

The global uptake of electric vehicles is driving demand for lithium-ion batteries with greater energy densities¹, hence the need for new cathodes with higher capacities². Lithium-rich cathode materials with lithium:transition metal (TM) ratios >1, including layered Li_{1+x}(Ni,Mn,Co)_{1-x}O₂ and disordered rocksalts such as Li₂MnO₂F, offer increased capacities over conventional cathodes such as LiCoO₂ and LiFePO₄^{3–5}. These high capacities are possible because Li-rich cathodes can exhibit reversible redox of bulk oxide ions, termed ‘oxygen-redox’, as well as transition metal ion redox^{9–11}. O-redox allows Li-rich cathode materials to achieve theoretical capacities exceeding 300 mA h g⁻¹ ref. 9, which opens up a new frontier in battery chemistry.

However, one critical issue is that O-redox is almost always associated with a large voltage hysteresis in the first-cycle electrochemical load curve^{12–17}. The degree to which fundamental atomic-scale mechanisms of O-redox in Li-rich cathodes contribute to voltage hysteresis is not fully understood and remains a topic of considerable

debate^{18–32}; in particular the nature of the oxidised O species formed on charge and the role of TM rearrangements are unclear³³. To harness Li-rich cathodes for technological use, the interrelations between O-redox, TM migration and voltage hysteresis must be fully understood so that strategies can be found to mitigate the loss of energy density.

The disordered rocksalt cathode Li₂MnO₂F exhibits a large capacity, comparable to that of Li-rich ordered layered oxides^{34,35}. Previous studies using resonant inelastic X-ray scattering (RIXS) and density functional theory (DFT) have identified molecular O₂ formed and trapped within the bulk structure when charged to 4.8 V (approximately Li_{0.75}MnO₂F)³⁵. Li₂MnO₂F and some other disordered rocksalts^{6,34,36–38} display a smaller first cycle voltage hysteresis than ordered layered cathode counterparts^{10,39}, which raises important questions: what is the atomic-scale O-redox mechanism within these disordered materials, and how does their local structure facilitate a more reversible O-redox process than in Li-rich layered cathode

¹Department of Chemistry, University of Bath, Bath, UK. ²The Faraday Institution, Harwell Science and Innovation Campus, Didcot, UK. ³Department of Materials, University of Oxford, Oxford, UK. ⁴Department of Chemistry, University of Oxford, Oxford, UK. ✉e-mail: saiful.islam@materials.ox.ac.uk

materials? In the highly ordered Li-rich layered cathodes, it is established that TM migration is necessary for O₂ formation^{14,16,21,22,40,41}. In disordered rocksalt materials such as Li₂MnO₂F, however, it is still unclear what role, if any, TM migration plays in O₂ formation.

To address these questions about transition metal migration, O₂ formation and voltage hysteresis in Li₂MnO₂F, we have conducted a multi-technique study of the charge-storage mechanism using DFT and ab initio molecular dynamics (AIMD) simulations, high-resolution RIXS mapping and galvanostatic intermittent titration technique (GITT) electrochemical measurements. Our DFT results reveal that in the highly charged (delithiated) state, molecular O₂ species are thermodynamically favoured over superoxide and peroxide species. This result is confirmed by new high-resolution RIXS mapping data, which shows vibrational features from molecular O₂ only, with no evidence for superoxide and peroxide species. Using AIMD, we resolve an O–O dimerisation mechanism that involves TM migration and features peroxide and superoxide species as short-lived (picosecond timescale) reaction intermediates, before ultimately forming the thermodynamic end-product, molecular O₂. We implicate irreversible Mn migration as a contributor to first cycle voltage hysteresis in Li₂MnO₂F and discuss how fully-reversible Mn migration could provide a route to stable O-redox cycling through O₂ formation without voltage loss.

Results

Oxygen environments and short-range order in Li₂MnO₂F

In disordered rocksalt-structured Li₂MnO₂F, octahedrally coordinated cations (Li, Mn) and anions (O, F) occupy two interpenetrating face-centred cubic (fcc) sublattices (Fig. 1a). Disordered rocksalts do not display long-range order, but do exhibit short-range cation order; i.e., preferential local structural motifs^{37,42–46}. Understanding how short-range order affects the local structure around oxygen anions in Li₂MnO₂F is important because O-redox activity in Li-rich cathodes has previously been attributed to the preferential oxidation of specific lattice O²⁻ ions with Li-rich coordination environments^{47–49}. O

ions with a higher number of Li neighbours have a lower Madelung site potential, which indicates a lower energy required to localise an electron hole (O²⁻ → O⁻ + e⁻)⁴⁹, while oxygen ions with linear Li–O–Li bonding configurations have O 2p states at the top of the valence band that are susceptible to oxidation on charge^{47,48}. Furthermore, the possible presence of extremely lithium-rich oxygen-coordination (i.e. O–Li₆) is of particular interest, because removal of these Li during charging may leave these O undercoordinated with no directly bonded Mn neighbours, and potentially allowing O–O dimerisation without requiring Mn–O bond breaking or Mn migration.

We first quantify the frequency of different oxygen coordination environments (O–Li₆, O–Li₅Mn, etc) in pristine, as-prepared Li₂MnO₂F. We used DFT calculations to parameterise a cluster-expansion Hamiltonian to describe the short-range interactions in Li₂MnO₂F and ran lattice Monte Carlo simulations at *T* = 2000 K to approximate the ball-milling synthesis conditions of the pristine, as-prepared material⁵⁴ (for computational details, see Methods section). Figure 1b shows the predicted frequencies of different O-ion coordination octahedra, O–Li_{*x*}Mn_{*6-x*}, obtained by sampling structures from these simulations. We also show data for a model at *T* = ∞ K, which represents a hypothetical fully random arrangement of the rocksalt lattice, i.e., with no short-range order (Supplementary Note S2.1).

The fully random (*T* = ∞ K) model of Li₂MnO₂F features a binomial distribution of O–Li_{*x*}Mn_{*6-x*} (Fig. 1b), which is skewed towards O-octahedra with a high number of Li neighbours due to the 2:1 ratio of Li:Mn in the material. In this fully random model, 8.5% of the O-environments are O–Li₆. In the system approximating the ball-milling synthesis conditions (*T* = 2000 K), the distribution of O-environments deviates from a fully random binomial distribution (Fig. 1b), which indicates short-range order in pristine Li₂MnO₂F. O–Li₆ environments are predicted to have a very low abundance (<0.05%), and F-ions preferentially occupy anion sites with high numbers of Li neighbours (Supplementary Fig. 1)^{43,45}. Because oxygen ions in O–Li₆ coordination appear with a very low frequency in the pristine material, the molecular O₂ that is observed in experiments upon cycling³⁴ cannot originate uniquely from starting O–Li₆ oxygen ion sites. Instead, the O₂ molecules must arise from O–Li_{*n*}Mn_{*6-n*} (where *n* ≤ 5) sites in the pristine material, or O–Li_{*x*}□_{*6-x*} configurations (where □ is a vacancy) that could form during charge due to O, Li or Mn displacement.

Stable structures and nature of oxidised oxygen on lithium extraction

Having characterised the anion short-range order in pristine Li₂MnO₂F, we now investigate the charge mechanism by examining structures of highly delithiated Li_{0.67}MnO₂F. This stoichiometry corresponds to structures charged past the limit of Mn³⁺ to Mn⁴⁺ redox and provide new insights into the thermodynamics of different oxidised O species and the possibility of Mn migration.

First, we perform a random structural search at a stoichiometry of Li_{0.67}MnO₂F by generating 150 rocksalt configurations with random distributions of anions and cations, plus cation vacancies, over their respective sublattices. This random structure search allows an unbiased sampling of all hypothetical rocksalt-structured configurations of Li_{0.67}MnO₂F, without imposing any conditions on the pristine Li₂MnO₂F structure or on the kinetic pathway that might be required to reach these delithiated structures in experimental samples. The random structure search therefore generated structures that could be obtained under unrestricted TM and anion rearrangement during charge; we label this the ‘Mn-rearrangement’ model. Second, we model delithiation of the pristine material, under the condition that no TM ion migration is permitted, denoted as the ‘constrained-Mn’ model. Here, we used our cluster expansion model at *T* = 2000 K to generate 150 Li₂MnO₂F structures, representative of the pristine material. These structures were delithiated either (i) by removing random lithium ions or (ii) removing Li based on a ranking of site energies from

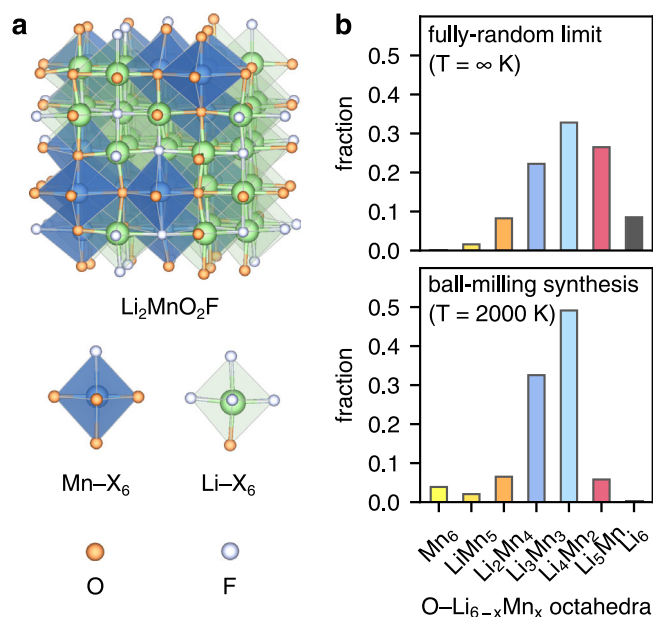


Fig. 1 | Structure and short-range order of Li₂MnO₂F. **a** Representative relaxed structure of disordered Li₂MnO₂F in a (2 × 2 × 2) expansion of the conventional rocksalt unit cell. **b** Frequency of O–Li_{*x*}Mn_{*6-x*} octahedra in Li₂MnO₂F at *T* = ∞ K (upper panel) derived from a binomial distribution with *n* = 6, *p* = 2/3, representing the fully-random limit and at *T* = 2000 K (lower panel) obtained from cluster-expansion based Monte Carlo simulations, representing the pristine ‘as-prepared’ material.

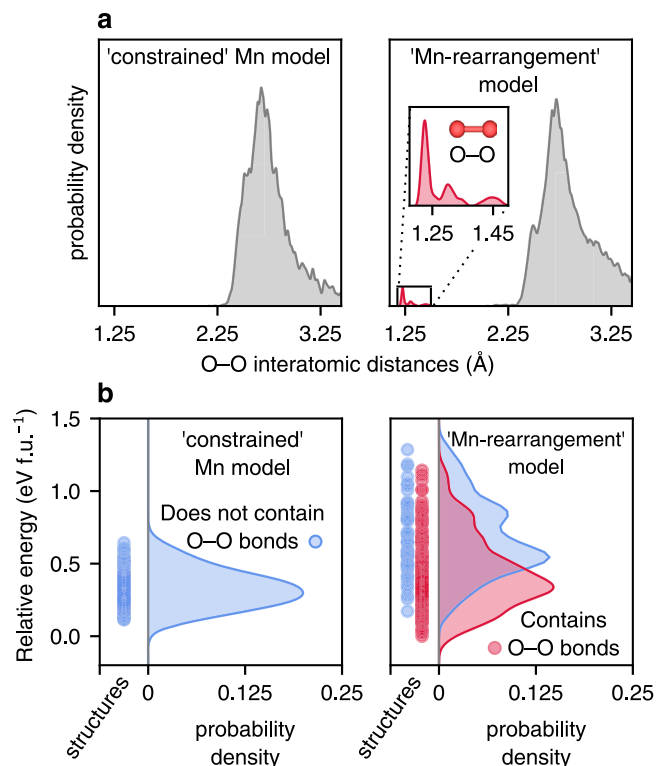


Fig. 2 | Search for O–O bonds and thermodynamics of O-dimer formation in delithiated $\text{Li}_{0.67}\text{MnO}_2\text{F}$. **a** Search for O–O dimers by an analysis of O–O interatomic distances in delithiated structures of the pristine material obtained from the cluster-expansion ('constrained' Mn), and in 'Mn rearrangement' models. **b** Energetics of the structures from **a** with the structures from the 'Mn-rearrangement' model separated into those containing O–O bonds (<1.7 Å) and those not containing O–O bonds. The right section of each panel shows the kernel density estimations of the probability of energies in the left panel, where each dot is the energy of one structure.

electrostatics, to reach a composition of $\text{Li}_{0.67}\text{MnO}_2\text{F}$ and then relaxed with DFT. The relaxations quench the structures to a local potential energy minimum and do not allow for significant atomic rearrangements such as Mn migration.

To assess whether O–O dimerisation occurs in any of the structures in either of the two models, we consider the distributions of O–O distances in the relaxed structures (Fig. 2a); distances shorter than 1.7 Å are indicative of covalent O–O dimerisation. In the constrained-Mn model structures, we find no O-dimers of any kind. Charge compensation beyond the Mn^{4+} limit in these models is predominantly from lattice O^{2-} ions. In contrast, a large proportion of structures from the Mn-rearrangement model show some O–O interatomic distances <1.7 Å, indicating short covalent O–O bonds (Fig. 2a).

Insight into the thermodynamics of O–O dimerisation in $\text{Li}_{0.67}\text{MnO}_2\text{F}$ is provided by considering the calculated energies of all the relaxed structures for the constrained Mn and Mn-rearrangement models (Fig. 2b). For the Mn-rearrangement model, structures that contain covalent O–O bonds are on average ~ 0.4 eV per formula unit more stable than those that do not contain covalent O–O bonds. Furthermore, the lowest energy structures across both models contain covalent O–O bonds. The results therefore suggest a thermodynamic driving force may exist for pristine $\text{Li}_2\text{MnO}_2\text{F}$ to undergo a framework transformation upon delithiation to allow O–O dimerisation.

The lack of dimerisation in the constrained Mn model is because O–O dimerisation is an activated process that requires either Mn–O bond breaking, or Mn/O displacement. All O atoms in the constrained Mn model start with at least one Mn neighbour, and the structures

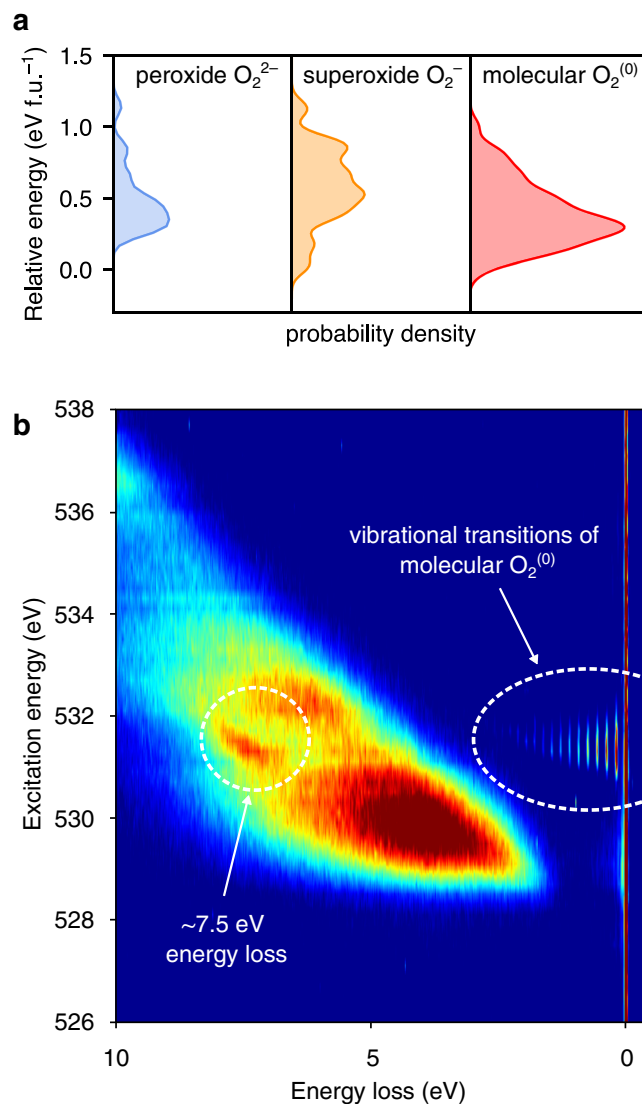


Fig. 3 | Computational and experimental evidence for molecular O_2 formation in charged $\text{Li}_{2-x}\text{MnO}_2\text{F}$. **a** Comparison of the stability of structures from the Mn rearrangement model, containing the different types of O–O dimers, classified according to bond length: (peroxide O_2^{2-} ($1.35 \text{ \AA} \leq d_{\text{O-O}} < 1.70 \text{ \AA}$), superoxide O_2^- ($1.24 \text{ \AA} \leq d_{\text{O-O}} < 1.35 \text{ \AA}$) and molecular O_2 ($d_{\text{O-O}} < 1.24 \text{ \AA}$)). The panels show the kernel density estimations of the probability of energies for the classified structures. The energies were calculated relative to the most stable configuration from the entire search. Thus, zero energy corresponds to the most stable obtained from the Mn rearrangement model. Calculations used the SCAN functional. **b** High-resolution resonant inelastic X-ray scattering (RIXS) map of $\text{Li}_{2-x}\text{MnO}_2\text{F}$ charged to 5.0 V, showing the vibrational features corresponding to molecular O_2 only, and an energy loss feature at ~ 7.5 eV.

relax to the nearest local energy minimum, rather than overcoming the barrier needed for O–O dimerisation. In contrast, in the Mn rearrangement model, some O atoms begin with no Mn neighbours and can dimerise without an activation barrier, so covalent O–O bonds ($d_{\text{O-O}} < 1.7$ Å) form during the geometry relaxations.

There is an ongoing debate over the bond length and oxidation state of O–O dimers in charged O-redox cathodes; peroxide O_2^{2-} ($d_{\text{O-O}} \sim 1.44$ Å) or $(\text{O}\cdots\text{O})^{n-}$ species with long interatomic separations of ~ 2.4 Å are sometimes invoked to explain capacity from oxidised $\text{O}^{11,21,50}$. In relaxed structures from the random structure search, the probability density for covalent O–O bonds has maxima at ~ 1.22 Å, ~ 1.30 Å and ~ 1.45 Å, (Fig. 2a, inset) indicating that molecular $\text{O}_2^{(0)}$, superoxide O_2^- and peroxide O_2^{2-} species could all form in $\text{Li}_{0.67}\text{MnO}_2\text{F}$. In Fig. 3a, we

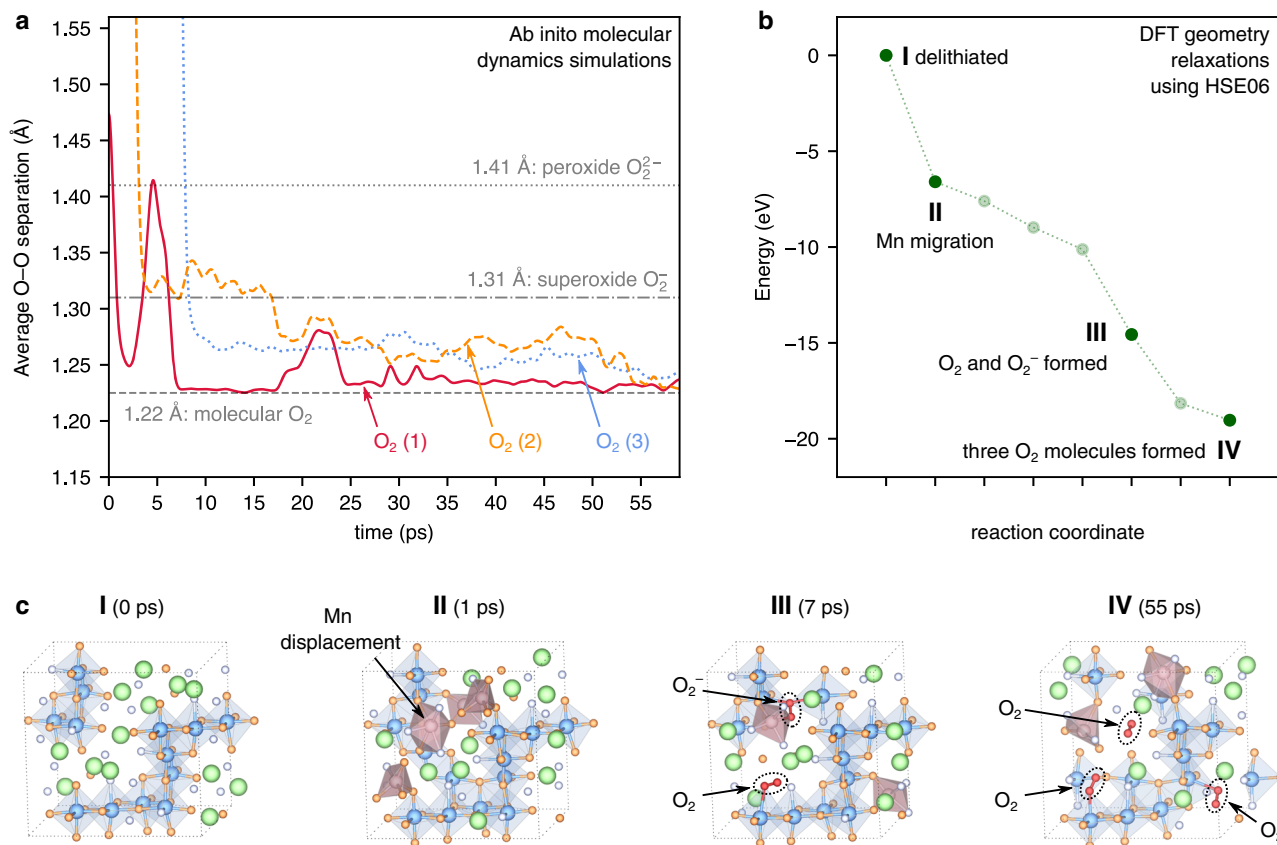


Fig. 4 | Reaction mechanism to form O–O dimers in $Li_{0.67}MnO_2F$ from ab initio molecular dynamics (AIMD) and geometry relaxations. **a** O–O interatomic separation of O species forming O–O dimers from GGA+*U* AIMD simulations at 500 K. **b** Total energy of selected structures along the AIMD trajectory, fully relaxed

with DFT using the HSE06 functional. **c** Geometry of the relaxed structures from **b**, indicating Mn migration events and O–O dimerisation. Mn ions displaced from their octahedrally coordinated rocksalt sites are indicated by pink polyhedra.

compare the thermodynamic stability of structures containing the different types of O–O dimers, classified, as is convention, according to bond length: (peroxide O_2^{2-} ($1.35 \text{ \AA} \leq d_{O-O} < 1.70 \text{ \AA}$), superoxide O_2^- ($1.24 \text{ \AA} \leq d_{O-O} < 1.35 \text{ \AA}$) and molecular O_2 ($d_{O-O} < 1.24 \text{ \AA}$))³¹. Structures containing molecular O_2 species are most frequently obtained and are, on average, the most stable, indicating that molecular O_2 is the thermodynamic product in charged Li_2MnO_2F .

To investigate the possible presence of peroxide or superoxide species in charged Li_2MnO_2F , we performed high-resolution O K-edge RIXS mapping of $Li_{2-x}MnO_2F$ charged to 5.0 V. In RIXS, incident radiation excites electrons from the O 1s core-level states to empty O 2p valence states, creating core-holes. Relaxation of electrons from the filled O 2p valence states back into the core hole (O 1s), results in emission photons, whose energy are measured, providing a direct probe of the oxygen valence states. The RIXS results are presented in terms of excitation energy, and (emission) energy loss. At an excitation energy of 531 eV, a series of energy loss features near the elastic (zero energy loss) peak can be resolved, arising from transitions to different vibrational energy levels of an O_2 molecule (Fig. 3b), with the peak separation of the lowest energy-loss peaks corresponding to the fundamental molecular O_2 vibrational frequency (ν) of 1550 cm^{-1} Refs. 14, 16, 52. No vibrational features from peroxide ($\nu = 750 \text{ cm}^{-1}$) or superoxide ($\nu = 1100 \text{ cm}^{-1}$) species are observed. The combined DFT and RIXS results support the idea that molecular O_2 is the thermodynamically favoured oxidised O product in highly delithiated Li_2MnO_2F , and in particular, highlight that molecular O_2 is favoured over peroxide and superoxide species.

Mechanism of O–O dimerisation in delithiated $Li_{2-x}MnO_2F$

The structural analysis presented above reveals a strong thermodynamic driving force for O_2 formation in highly delithiated $Li_{0.67}MnO_2F$, which is consistent with the experimental observation of molecular O_2 trapped in the bulk structure³⁵, and also highlights the necessary role of Mn, O or F migration for this O-redox process to occur. Although this analysis provides valuable thermodynamic insights, it does not give direct information about the atomic mechanisms involved.

We therefore performed ab initio molecular dynamics (AIMD) simulations on a selection of delithiated structures, which allows us to probe their structural evolution as a function of time^{53,54}. We examined nine different charged $Li_{0.67}MnO_2F$ structures, which were obtained as Li_2MnO_2F from the cluster-expansion, then delithiated (see Methods section). We ran AIMD simulations on each structure at 500 K, a slightly elevated temperature with respect to experiment to allow better sampling of kinetically allowed processes within the accessible simulation timescale (~60 ps). For our detailed analysis here, we focus on one exemplar structure (Fig. 4); structures for the other simulations are shown in the Supplementary Information (Supplementary Fig. 7).

Within this simulation trajectory, three O_2 molecules form spontaneously. Further analysis highlights three key points. First, we show that molecular O_2 formation is preceded by Mn ion migration (Fig. 4c), with several Mn ions migrating from their initial octahedrally coordinated sites to interstitial sites. These are either also octahedrally coordinated sites, located at the shared edge between two pairs of octahedral sites in the original rocksalt lattice or are fivefold coordinated sites. The displaced Mn ions are stabilised in these interstitial

positions due to large off-site relaxations of the anion sublattice (Supplementary Fig. 8). Second, these Mn migration events leave some O ions in undercoordinated environments (fewer than two Mn nearest-neighbours); a concurrent displacement of the anion sublattice allows some O ions to approach each other which then permits O–O dimerisation. Third, the mechanism to form molecular O₂ involves peroxide and superoxide species appearing as short-lived (picosecond timescale) reaction intermediates; details of these intermediate O₂ⁿ⁻ species can be resolved by tracking the O–O interatomic separation of the pairs of O that form the O₂ molecules (Fig. 4a).

Closer analysis shows that the formation of molecule O₂(1) involves rapid dimerisation (within 2 ps), briefly appearing as a peroxide intermediate with an O–O bond of 1.40 Å, before detaching from neighbouring Mn ions and relaxing to molecular O₂ (*d*_{O–O} = 1.22 Å). O₂(1) can be classified clearly as molecular O₂ for the majority of the 60 ps simulation, except for a brief interaction with framework O atoms (Supplementary Fig. 9), which cause temporary (~4 ps) lengthening of the O–O distance to ~1.30 Å (superoxide).

The formation of molecules O₂(2) and O₂(3) shows different behaviour; these dimerise after 3 ps and 7.5 ps respectively, and initially bridge between two or three Mn ions (Supplementary Fig. 5). Molecule O₂(2) initially has a O–O separation of ~1.3 Å, corresponding to a superoxide species, before shortening slightly to an average of 1.25 Å, which is intermediate between the equilibrium superoxide O–O distance and molecular O₂ species. Molecules O₂(2) and O₂(3) remain in this intermediate state, until ~55 ps, at which point the O–O distances for both dimers shorten to 1.22 Å (molecular O₂), coinciding with each dimer moving away from their neighbouring Mn ions, into a Li-vacancy nanovoid in the structure.

The change in potential energy that accompanies this process of coupled Mn-migration and molecular O₂ formation is illustrated in Fig. 4b, which shows DFT energies for selected structures along the AIMD trajectory that were fully relaxed at the hybrid functional level. Each selected structure relaxes to a local energy minimum, and following the reaction pathway leads to an overall stabilisation of the system. The superoxide species found in the AIMD simulations are found to be short-lived metastable reaction intermediates on a ps timescale, and exist in a shallow potential well on the energy surface, in agreement with the observation of some superoxide species from the random structure search (Fig. 2). The final product along the AIMD trajectory, containing molecular O₂ is confirmed to be the most stable configuration, in agreement with the experimental RIXS data (Fig. 3).

Charge-discharge process and voltage hysteresis

Understanding the important relationship between voltage hysteresis, TM migration and O₂ formation in Li-rich cathodes requires investigating both the charge and discharge processes, and considering possible structural changes during the first cycle. Our results show that in Li₂MnO₂F, molecular O₂ formation at the top of charge drives a reconfiguration of the cathode Mn-host framework. This may then lead to a different reaction pathway and different energetics for discharge compared to charge, and a new structure after the first cycle.

To investigate the role of molecular O₂ formation and Mn-migration in voltage hysteresis, we calculated the voltage curve upon charging to Li_{0.67}MnO₂F, considering the following two possible alternative end-points (i) metastable structures containing lattice Oⁿ⁻ ions, and (ii) a structure containing O₂. The structures containing lattice Oⁿ⁻ ions were obtained by removing Li from the pristine Mn-host framework. The structure containing O₂ was obtained by taking the most stable structure containing Oⁿ⁻ and performing the minimum number of Mn hops that would leave an O atom undercoordinated and allow O₂ to form (Fig. 5). The calculated charge voltage curves were compared with an experimental first charge/discharge curve obtained from GITT measurements (see Methods section). GITT provides a

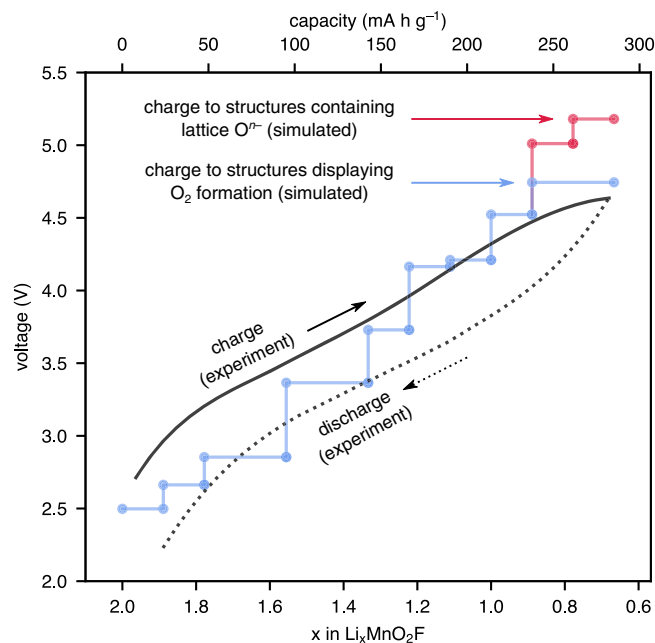


Fig. 5 | Experimental and calculated voltage curves. The calculations are based on charging to structures containing lattice Oⁿ⁻, or to a structure containing O₂, compared against the experimental first-cycle voltage-capacity curve from galvanostatic intermittent titration technique (GITT) measurements.

voltage profile much closer to the thermodynamic equilibrium than cycling at a conventional C-rate (i.e. 0.1 C).

The results in Fig. 5 reveal two key features. First, the calculated charge voltage curve to structures containing lattice Oⁿ⁻ ions exceeds 5 V, which is clearly inconsistent with experiment. Second, the delithiated structure containing O₂ has a lower predicted voltage, providing a better agreement with experiment. The average calculated charge voltage from the pristine structure to the structure containing O₂ is 3.65 V (Supplementary Note S2.3), which compares well with the average experimental voltage of 3.65 V.

We then investigated the discharge process and how this is affected by a structural rearrangement during charge, by re-inserting lithium ions back into the structure containing O₂ and calculating the average discharge voltage. Re-inserting Li into the structure containing O₂ results in a new discharged structure that contains two O–Li₆ environments; the O atoms of the O₂ molecule formed during charge are re-incorporated into the lattice as Oⁿ⁻ ions. This new discharged structure is significantly higher in energy (~0.4 eV f.u.⁻¹) than the pristine Li₂MnO₂F structure, due to the relative instability of the trapped O–Li₆ environments (Supplementary Fig. 18). The average calculated discharge voltage is 3.35 V; this is 0.3 V lower than the calculated charge voltage, in accord with the ~0.16 V hysteresis observed experimentally from a mid-point potential rest experiment (Supplementary Fig. 20). In other words, the calculations indicate there is a voltage hysteresis, and this arises from the irreversible structural transformation during charge to form O₂.

Strategies to harness reversible O-redox

Preventing voltage hysteresis and voltage fade is critical for the development of practical O-redox cathodes with high energy densities. Hysteresis can have several sources, including kinetic limitations such as cathode polarisation due to slow lithium diffusion, or first-order phase transitions, both of which should disappear in the limit of extremely slow charging rates, where thermodynamic equilibrium is approached. Another type is ‘path-dependent’ hysteresis which can arise from irreversible structural changes or slow mobility of host TM cation or anion species⁵⁵. One strategy proposed¹⁸ to suppress

path-dependent hysteresis in O-redox cathodes is to prevent O₂ formation by inhibiting TM migration^{16,56,57}. In our AIMD simulations, we observe several Mn migration events. Mn migration occurs when Li ions are removed from the structure adjacent to Mn, and the Mn ions then move into new sites, made possible by these vacancies. The relatively large number of Mn ions that migrate is because there are many lithium vacancies at high levels of delithiation in such a lithium-rich system Li₂MnO₂F. This implicit link between high Li:TM ratios and ease of Mn migration implies a trade-off in disordered rocksalt cathodes between theoretical capacity and preventing voltage hysteresis. Lower levels of Li-excess, and a more contiguous and connected 3D framework of edge-sharing TM ions is expected to help prevent TM migration.

A similar principle has been proposed in layered Li-rich cathodes, where the superstructure ordering within TM layers affects the stability of those layers; greater stability is achieved with more contiguous TM connectivity¹⁶. Interesting 3D examples that illustrate this principle include ‘partially ordered’ spinel-type Mn-oxyluoride cathodes, which display small voltage hysteresis³⁸. These spinel-type materials have a relatively low Li:TM ratio (~1.5 compared with 2 here in Li₂MnO₂F), which is likely to have a relatively well-connected network of edge-sharing Mn octahedra. We suggest that these features will tend to reduce the magnitude of off-lattice anion displacements at high states of charge and inhibit TM migration. Achieving a lower level of Li-excess in Li₂MnO₂F, if the level of fluorination is kept constant, opens the possibility of using low-valent dopants such as Mg²⁺ and Zn²⁺⁵⁸, in contrast to high-valent d⁰ dopants such as Ti⁴⁺ and Nb⁵⁺ that are often used in disordered rocksalt cathodes³⁹.

Another approach to the design of Li-rich disordered rocksalt cathodes would be to allow O₂ formation and then aim to have fully-reversible TM migration, where the TM ions return to their original sites¹⁸. By allowing O₂ formation, the cathode is rendered much more stable on charge, since metastable lattice O^{•-} species are not trapped in the structure. To allow O₂ formation, the roles of local structural rearrangements and reversible transition ion migration become important. The displacement of octahedral cations into tetrahedral sites, as has recently been described for Cr³⁺ to Cr⁶⁺ in the disordered rocksalt cathodes Li_{1.2}Mn_{0.2}Ti_{0.4}Cr_{0.2}O₂ ref. 59 and Li₂Mn_{0.75}Cr_{0.25}O₂F ref. 60, and for Fe ions in Li_{1.17}Ti_{0.33}Fe_{0.5}O₂ ref. 15 may permit O–O dimerisation while partially recovering the original structure on discharge. In our study, we show that large off-lattice displacements of anions can permit the migration of Mn ions into interstitial sites. Fully-reversible migration of these Mn ions back to their original sites on discharge could recover the starting structure, and may result in suppressed voltage hysteresis⁶¹.

Discussion

In conclusion, we have shown that, despite exhibiting limited structural order, Li-rich disordered rocksalt cathodes such as Li₂MnO₂F, require transition metal migration before molecular O₂ is able to form in the bulk structure on charge. Our results unify the behaviour of disordered rocksalt cathodes with Li-rich ordered layered cathodes, where it is already known that the O-redox process also involves transition metal migration and O₂ formation, leading to voltage hysteresis. The nature of hysteresis in disordered materials does differ from the layered systems, since they exhibit solid solution rather than two-phase behaviour during the first charge. Hence, Mn migration and O₂ formation occur throughout the rocksalt rather than only in a fraction of the layered cathode that is charged.

Ab initio molecular dynamics combined with DFT calculations show that both TM migration and O₂ formation are thermodynamically favoured processes and occur rapidly in charged Li₂MnO₂F. High-resolution RIXS mapping confirms that molecular O₂ forms (rather than superoxide or peroxide species) and is trapped within lithium vacancy clusters or nanovoids in the bulk material. On discharge, the

O₂ molecules are reduced back to O²⁻ lattice ions. When migration is irreversible, these O²⁻ ions occupy sites with a different coordination environment than the pristine compound, which leads to a loss of voltage (~0.3 V) in the first charge/discharge cycle, consistent with the degree of voltage hysteresis observed experimentally. If Mn displacement is fully-reversible, the original Li₂MnO₂F structure and coordination around O²⁻ are recovered, which facilitates O-redox cycling without path-dependent voltage hysteresis. The results presented here suggest that promoting reversible transition metal displacement or suppressing migration altogether in Li-rich disordered rocksalt cathode materials would provide effective strategies to harness O-redox without loss of energy density.

Data availability

The datasets generated during and/or analysed during the current study are available in the University of Bath repository (<https://doi.org/10.15125/BATH-01189>).

Code availability

All code used in this work is described in the Methods section and is openly available.

References

1. Liu, Y., Zhu, Y. & Cui, Y. Challenges and opportunities towards fast-charging battery materials. *Nat. Energy* **4**, 540–550 (2019).
2. Rozier, P. & Tarascon, J. M. Review — Li-rich layered oxide cathodes for next-generation Li-ion batteries: chances and challenges. *J. Electrochem. Soc.* **162**, A2490–A2499 (2015).
3. Li, X. et al. A new type of Li-rich rock-salt oxide Li₂Ni_{1/3}Ru_{2/3}O₃ with reversible anionic redox chemistry. *Adv. Mater.* **31**, 1807825 (2019).
4. Crafton, M. J., Yue, Y., Huang, T.-Y., Tong, W. & McCloskey, B. D. Anion reactivity in cation-disordered rocksalt cathode materials: the influence of fluorine substitution. *Adv. Energy Mater.* **10**, 2001500 (2020).
5. Källquist, I. et al. Degradation mechanisms in Li₂VO₂F Li-rich disordered rock-salt cathodes. *Chem. Mater.* **31**, 6084–6096 (2019).
6. Chen, R. et al. Disordered lithium-rich oxyfluoride as a stable host for enhanced Li⁺ intercalation storage. *Adv. Energy Mater.* **5**, 1401814 (2015).
7. Yabuuchi, N. et al. High-capacity electrode materials for rechargeable lithium batteries: Li₃NbO₄-based system with cation-disordered rocksalt structure. *Proc. Natl Acad. Sci. USA* **112**, 7650 (2015).
8. Hu, E. et al. Evolution of redox couples in Li- and Mn-rich cathode materials and mitigation of voltage fade by reducing oxygen release. *Nat. Energy* **3**, 690–698 (2018).
9. Assat, G. & Tarascon, J.-M. Fundamental understanding and practical challenges of anionic redox activity in Li-ion batteries. *Nat. Energy* **3**, 373–386 (2018).
10. Yabuuchi, N. Material design concept of lithium-excess electrode materials with rocksalt-related structures for rechargeable non-aqueous batteries. *Chem. Rec.* **19**, 690–707 (2019).
11. Ben Yahia, M., Vergnet, J., Saubanère, M. & Doublet, M.-L. Unified picture of anionic redox in Li/Na-ion batteries. *Nat. Mater.* **18**, 496–502 (2019).
12. Croy, J. R., Gallagher, K. G., Balasubramanian, M., Long, B. R. & Thackeray, M. M. Quantifying hysteresis and voltage fade in xLi₂MnO₃-(1-x)LiMn_{0.5}Ni_{0.5}O₂ electrodes as a function of Li₂MnO₃ content. *J. Electrochem. Soc.* **161**, A318–A325 (2013).
13. Jacquet, Q. et al. Charge transfer band gap as an indicator of hysteresis in Li-disordered rock salt cathodes for Li-ion batteries. *J. Am. Chem. Soc.* **141**, 11452–11464 (2019).
14. House, R. A. et al. First-cycle voltage hysteresis in Li-rich 3d cathodes associated with molecular O₂ trapped in the bulk. *Nat. Energy* **5**, 777–785 (2020).

15. Li, B. et al. Correlating ligand-to-metal charge transfer with voltage hysteresis in a Li-rich rock-salt compound exhibiting anionic redox. *Nat. Chem.* **13**, 1070–1080 (2021).
16. House, R. A. et al. Superstructure control of first-cycle voltage hysteresis in oxygen-redox cathodes. *Nature* **577**, 502–508 (2020).
17. Taylor, Z. N. et al. Stabilization of O–O bonds by d⁰ cations in Li_{4+x}Ni_{1-x}WO₆ (0 ≤ x ≤ 0.25) rock salt oxides as the origin of large voltage hysteresis. *J. Am. Chem. Soc.* **141**, 7333–7346 (2019).
18. House, R. A. et al. The role of O₂ in O-redox cathodes for Li-ion batteries. *Nat. Energy* **6**, 781–789 (2021).
19. Yabuuchi, N. et al. Origin of stabilization and destabilization in solid-state redox reaction of oxide ions for lithium-ion batteries. *Nat. Commun.* **7**, 13814 (2016).
20. Radin, M. D., Vinckeviciute, J., Seshadri, R. & Van der Ven, A. Manganese oxidation as the origin of the anomalous capacity of Mn-containing Li-excess cathode materials. *Nat. Energy* **4**, 639–646 (2019).
21. Hong, J. et al. Metal–oxygen decoordination stabilizes anion redox in Li-rich oxides. *Nat. Mater.* **18**, 256–265 (2019).
22. Gent, W. E. et al. Coupling between oxygen redox and cation migration explains unusual electrochemistry in lithium-rich layered oxides. *Nat. Commun.* **8**, 2091 (2017).
23. Baur, C. et al. Improved cycling stability in high-capacity Li-rich vanadium containing disordered rock salt oxyfluoride cathodes. *J. Mater. Chem. A* **7**, 21244–21253 (2019).
24. Yao Z, Kim S, He J, Hegde V L., & Wolverton C. Interplay of cation and anion redox in Li₄Mn₂O₅ cathode material and prediction of improved Li₄(Mn,M)₂O₅ electrodes for Li-ion batteries. *Sci. Adv.* **4**, eaa06754 (2018).
25. Yue, Y. et al. Redox behaviors in a Li-excess cation-disordered Mn–Nb–O–F rocksalt cathode. *Chem. Mater.* **32**, 4490–4498 (2020).
26. Chang, J. H. et al. Superoxide formation in Li₂VO₂F cathode material – a combined computational and experimental investigation of anionic redox activity. *J. Mater. Chem. A* **8**, 16551–16559 (2020).
27. Chen, D., Kan, W. H. & Chen, G. Understanding performance degradation in cation-disordered rock-salt oxide cathodes. *Adv. Energy Mater.* **9**, 1901255 (2019).
28. Yue, Y. et al. Tailoring the redox reactions for high-capacity cycling of cation-disordered rocksalt cathodes. *Adv. Funct. Mater.* **31**, 2008696 (2021).
29. Chung, H. et al. Experimental considerations to study Li-excess disordered rock salt cathode materials. *J. Mater. Chem. A* **9**, 1720–1732 (2021).
30. Lee, H. et al. Impact of local separation on the structural and electrochemical behaviors in Li₂MoO₃·LiCrO₂ disordered rock-salt cathode material. *Adv. Energy Mater.* **11**, 2002958 (2021).
31. Naylor, A. J. et al. Stabilization of Li-rich disordered rocksalt oxyfluoride cathodes by particle surface modification. *ACS Appl. Energy Mater.* **3**, 5937–5948 (2020).
32. Serrano-Sevillano, J., Carlier, D., Saracibar, A., Lopez del Amo, J. M. & Casas-Cabanas, M. DFT-assisted solid-state NMR characterization of defects in Li₂MnO₃. *Inorg. Chem.* **58**, 8347–8356 (2019).
33. Zhang, M. et al. Pushing the limit of 3d transition metal-based layered oxides that use both cation and anion redox for energy storage. *Nat. Rev. Mater.* **7**, 522–540 (2022).
34. House, R. A. et al. Lithium manganese oxyfluoride as a new cathode material exhibiting oxygen redox. *Energy Environ. Sci.* **11**, 926–932 (2018).
35. Sharpe, R. et al. Redox chemistry and the role of trapped molecular O₂ in Li-rich disordered rocksalt oxyfluoride cathodes. *J. Am. Chem. Soc.* **142**, 21799–21809 (2020).
36. Lee, J. et al. Reversible Mn²⁺/Mn⁴⁺ double redox in lithium-excess cathode materials. *Nature* **556**, 185–190 (2018).
37. Lun, Z. et al. Design principles for high-capacity Mn-based cation-disordered rocksalt cathodes. *Chem* **6**, 153–168 (2020).
38. Ji, H. et al. Ultrahigh power and energy density in partially ordered lithium-ion cathode materials. *Nat. Energy* **5**, 213–221 (2020).
39. Clément, R. J., Lun, Z. & Ceder, G. Cation-disordered rocksalt transition metal oxides and oxyfluorides for high energy lithium-ion cathodes. *Energy Environ. Sci.* **13**, 345–373 (2020).
40. Gent, W. E., Abate, I. I., Yang, W., Nazar, L. F. & Chueh, W. C. Design rules for high-valent redox in intercalation electrodes. *Joule* **4**, 1369–1397 (2020).
41. Boivin, E. et al. Bulk O₂ formation and Mg displacement explain O-redox in Na_{0.67}Mn_{0.72}Mg_{0.28}O₂. *Joule* **5**, 1267–1280 (2021).
42. Ji, H. et al. Hidden structural and chemical order controls lithium transport in cation-disordered oxides for rechargeable batteries. *Nat. Commun.* **10**, 592 (2019).
43. Clément, R. J., Kitchaev, D., Lee, J. & Ceder, G. Short-range order and unusual modes of nickel redox in a fluorine-substituted disordered rocksalt oxide lithium-ion cathode. *Chem. Mater.* **30**, 6945–6956 (2018).
44. Mozzhukhina, N. et al. Short-range ordering in the Li-rich disordered rock salt cathode material Li₂VO₂F revealed by Raman spectroscopy. *J. Raman Spectrosc.* **51**, 2095–2101 (2020).
45. Ouyang, B. et al. Effect of fluorination on lithium transport and short-range order in disordered-rocksalt-type lithium-ion battery cathodes. *Adv. Energy Mater.* **10**, 1903240 (2020).
46. Richards, W. D., Dacek, S. T., Kitchaev, D. A. & Ceder, G. Fluorination of lithium-excess transition metal oxide cathode materials. *Adv. Energy Mater.* **8**, 1701533 (2018).
47. Seo, D.-H. et al. The structural and chemical origin of the oxygen redox activity in layered and cation-disordered Li-excess cathode materials. *Nat. Chem.* **8**, 692–697 (2016).
48. Luo, K. et al. Charge-compensation in 3d-transition-metal-oxide intercalation cathodes through the generation of localized electron holes on oxygen. *Nat. Chem.* **8**, 684–691 (2016).
49. Davies, D. W., Morgan, B. J., Scanlon, D. O. & Walsh, A. Low-cost descriptors of electrostatic and electronic contributions to anion redox activity in batteries. *IOPSciNotes* **1**, 024805 (2020).
50. Sathiya, M. et al. Reversible anionic redox chemistry in high-capacity layered-oxide electrodes. *Nat. Mater.* **12**, 827–835 (2013).
51. Vinckeviciute, J., Kitchaev, D. A. & Van der Ven, A. A Two-step oxidation mechanism controlled by Mn migration explains the first-cycle activation behavior of Li₂MnO₃-based Li-excess materials. *Chem. Mater.* **33**, 1625–1636 (2021).
52. House, R. A. et al. Covalency does not suppress O₂ formation in 4d and 5d Li-rich O-redox cathodes. *Nat. Commun.* **12**, 2975 (2021).
53. Croy, J. R. et al. First-charge instabilities of layered-layered lithium-ion-battery materials. *Phys. Chem. Chem. Phys.* **17**, 24382–24391 (2015).
54. Zhang, Z., Zhao, S., Wang, B. & Yu, H. Local redox reaction of high valence manganese in Li₂MnO₃-based lithium battery cathodes. *Cell Rep. Phys. Sci.* **1**, 100061 (2020).
55. Van der Ven, A., See, K. A. & Pilon, L. Hysteresis in electrochemical systems. *Battery Energy*, <https://doi.org/10.1002/bte2.20210017> (2022).
56. Kitchaev, D. A., Vinckeviciute, J. & Van der Ven, A. Delocalized metal–oxygen π-redox is the origin of anomalous nonhysteretic capacity in Li-ion and Na-ion cathode materials. *J. Am. Chem. Soc.* **143**, 1908–1916 (2021).
57. Abate, I. I. et al. Coulombically-stabilized oxygen hole polarons enable fully reversible oxygen redox. *Energy Environ. Sci.* **14**, 4858–4867 (2021).
58. Zhong, P. et al. Increasing capacity in disordered rocksalt cathodes by Mg doping. *Chem. Mater.* **32**, 10728–10736 (2020).

59. Huang, J. et al. Non-topotactic reactions enable high rate capability in Li-rich cathode materials. *Nat. Energy* **6**, 706–714 (2021).
60. Zheng, X. et al. Reversible Mn/Cr dual redox in cation-disordered Li-excess cathode materials for stable lithium ion batteries. *Acta Mater.* **212**, 116935 (2021).
61. Eum, D. et al. Voltage decay and redox asymmetry mitigation by reversible cation migration in lithium-rich layered oxide electrodes. *Nat. Mater.* **19**, 419–427 (2020).

Acknowledgements

The authors thank the Faraday Institution CATMAT project (EP/S003053/1, FIRG016) and the Henry Royce Institute for financial support. We are also grateful to the HEC Materials Chemistry Consortium (EP/R029431) for Archer high-performance computing (HPC) facilities, GW4 and the UK Met Office for access to the Isambard HPC Service (EP/P020224/1) and for the Faraday Institution's MICHAEL HPC resource. K.M. and A.G.S. thank Dr Stefano Angioni for access to HPC resources through the University of Bath's Cloud Computing Pilot Project. A.G.S. thanks the STFC Batteries Network for an Early Career Researcher Award (ST/R006873/1). This project was supported by the Royal Academy of Engineering under the Research Fellowship scheme. B.J.M. acknowledges support from the Royal Society (URF\R\191006). We acknowledge Diamond Light Source for time on I21 under proposal MM29028-1.

Author contributions

K.M., B.J.M. and M.S.I. conceived the work. K.M. performed and analysed the calculations with input from A.S. and S.C.; B.J.M. and M.S.I. supervised the computational work. R.A.H. and G.J.R. collected the RIXS measurements and performed the electrochemistry. P.B. supervised the experimental work. K.M., B.J.M. and M.S.I. wrote the manuscript with contributions from all authors.

Competing interests

The authors declare no competing interests.

Additional information

Supplementary information The online version contains supplementary material available at <https://doi.org/10.1038/s41467-022-32983-w>.

Correspondence and requests for materials should be addressed to M. Saiful Islam.

Peer review information *Nature Communications* thanks Bingwen Hu and the other, anonymous, reviewer(s) for their contribution to the peer review of this work. Peer reviewer reports are available.

Reprints and permission information is available at <http://www.nature.com/reprints>

Publisher's note Springer Nature remains neutral with regard to jurisdictional claims in published maps and institutional affiliations.

Open Access This article is licensed under a Creative Commons Attribution 4.0 International License, which permits use, sharing, adaptation, distribution and reproduction in any medium or format, as long as you give appropriate credit to the original author(s) and the source, provide a link to the Creative Commons license, and indicate if changes were made. The images or other third party material in this article are included in the article's Creative Commons license, unless indicated otherwise in a credit line to the material. If material is not included in the article's Creative Commons license and your intended use is not permitted by statutory regulation or exceeds the permitted use, you will need to obtain permission directly from the copyright holder. To view a copy of this license, visit <http://creativecommons.org/licenses/by/4.0/>.

© The Author(s) 2022